ISIJ International, Vol. 54 (2014), No. 10, pp. 2324–2333

Analysis of Transient Transport and Entrapment of Particle in Continuous Casting Mold

Zhongqiu LIU,[1)] Baokuan LI,[1)]* Li ZHANG[2)] and Guodong XU[2)]

1) School of Materials and Metallurgy, Northeastern University, No. 3-11 Wenhua road, Heping District, Shenyang, 110819 China.
2) Baoshan Iron & Steel Co., Ltd., No. 885 Fujin Road, Baoshan District, Shanghai, 201900 China.

(*Received on April 1, 2014; accepted on June 3, 2014*)

A mathematical model has been developed to simulate the transient turbulent flow, solidification, transport and entrapment of particles in a continuous casting mold. The turbulence of molten steel inside the liquid pool is calculated using the large eddy simulation (LES). The enthalpy-porosity approach is used to simulate the solidification of steel. A Laplacian equation is used to approximate the pull velocity in the solid region. The transport of particle (bubble and non-metallic inclusion) inside the liquid pool is considered according to the Lagrangian approach. A criterion for particle entrapment in the solidified front is developed using the user-defined functions (UDF) of FLUENT software, considering force balance involving eight different forces acting on a particle at the mushy-zone. The predicted asymmetrical flow pattern is compared with the water model experiment results. The entrapped positions of particles in the solidified shell are predicted and compared with the ultrasonic flaw results of rolled steel plates and the previous study of inclusions distribution in slabs. The model has successfully reproduced many known phenomena and other new predictions, including the transient asymmetrical flow pattern, transient asymmetrical distribution of particles inside the liquid pool, transient entrapment ratios and asymmetrical positions of different particles in the solidified shell.

KEY WORDS: continuous casting mold; solidification; particle transport and entrapment; large eddy simulation.

1. Introduction

With the development of engineering and continuous improvement in rolling processes, higher requirements of steel product quality are brought forward by many industries. For example, the production of modern high-quality automobile body sheets and pipe steels, calls for better control the surface quality of the billets. And it is essential to reduce the internal defects inside the slabs for producing boiler steels and ship plate steels. These defects[1–3)] in slabs and rolled steel plates, such as slip crack, slivers and blisters, are often caused by captured non-metallic inclusions, slag and bubbles, as shown in **Fig. 1**. Through the LF, RH and tundish refining, most of large non-metallic inclusions have been removed and the purity of molten steel has been raised. However, many smaller non-metallic inclusions still stay inside the molten steel, would be carried deep into the mold later, and collide together to form larger clusters, as shown in Fig. 1(c).[3)] Another important source of non-metallic inclusions is the entrainment of slag into the molten steel, which would produce large spherical inclusions (Fig. 1(d)).[3)] Argon gas is injected into the submerged entrance nozzle (SEN) to prevent nozzle clogging and remove the non-metallic inclusions in the mold. Large bubbles will escape from the top surface safely, but some smaller bubbles (usually surrounded by inclusions) will be harmfully entrapped by the solidified shell, causing pinhole defects, as shown in Fig. 1(e).[4)] Therefore, in order to improve steel quality, it is essential to study and predict the transport and entrapment of particles (bubbles and non-metallic inclusions) in the continuous casting processes.

During continuous casting processes, the transport and entrapment of particles mainly depend on the turbulent fluid flow, solute concentration, temperature, and solidification of steel in the mold. Extensive studies of the effect of turbulent fluid flow on particle transport and entrapment inside the mold have been performed on physical modeling[5–8)] and mathematical simulation.[9–13)] Kwon *et al.*[7)] studied the inclusions removed by bubble adhesion in continuous casting mold respectively using the water model and mathematical model, finding the wettability of inclusions with liquid is a decisive factor in inclusion removal. Yuan *et al.*[9)] simulated the transient fluid flow of steel in a slab using the large eddy simulation (LES) and compared the results with the flow fields of water measured with DPIV technology, finding good agreement between both of data. And the flow fields were used to investigate the transport of particles. Many studies on the entrapment of particles at the solidifying interface have been done. Some workers[14–18)] considered the effect of surface tension gradient induced forces (Marangoni force) due to the gradient of solute concentration and temperature. Mukai and Lin[14–16)] simulated the motion of fine bubbles under a solute concentration gradient (solute Marangoni force). However, the continuous casting process is basically cooling process, so Lee *et al.*[18)] proposed a dynamic model of particle entrapment on studying the effect of thermal Marangoni force, indicating that the thermal Marangoni force plays an important role, and this model predicts the particle behavior in the solid/liquid interface more precisely. Thomas *et al.*[19)] derived a balance of various forces acting on a particle in the boundary layer, and

* Corresponding author: E-mail: libk@smm.neu.edu.cn
DOI: http://dx.doi.org/10.2355/isijinternational.54.2324

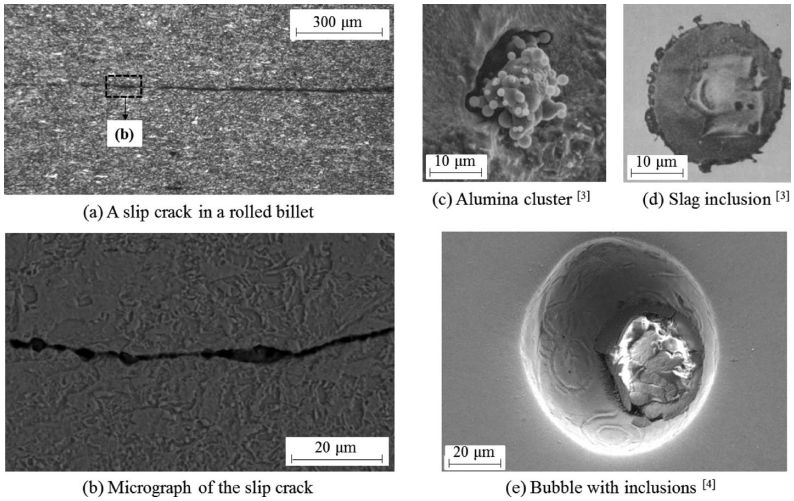

(a) A slip crack in a rolled billet
(c) Alumina cluster [3]
(d) Slag inclusion [3]
(b) Micrograph of the slip crack
(e) Bubble with inclusions [4]

Fig. 1. Example of slip crack in a rolled billet and different types of particles entrapped during steel casting.

the primary dendrite arm spacing (PDAS) was considered for the particle entrapment. The solidified shell was precalculated via the square root law. Yuji Miki *et al.*[20] used a model experiment studying the entrapment of particles on the solidified shell using molten steel, finding that the entrapment of particles is greatly reduced by the existence of a low velocity flow, *e.g.*, 0.05 m/s.

The asymmetrical and unsteady distribution of defects has been found in recent flaw detection of slabs[21] and steel plates.[22] A number of workers also reported that the fluid flow pattern inside the mold is not symmetrical along the central plane, and not stationary. However, in any case, most of the mathematical simulations reported in the literatures used the Reynolds-averaged turbulence models (mainly the k-ε model) to study the flow in the mold, poorly estimating the turbulent dynamics information. The LES model was successfully applied to obtain the transient and asymmetrical flow of molten steel in the mold,[9,13,22] but not including the solidification process.

The present work develops a mathematical model for investigating the transient turbulent flow of molten steel, solidification of steel, and transport and entrapment of particles in the continuous casting mold. The predicted asymmetrical flow patterns are compared with the water model experiment results. Inclusion distributions of in situ observation at steel plates, which have been handled with slab scarfing machine, are carried out by using an ultrasonic flaw detector. The entrapped positions of particles in the cross sections of steel slab are predicted and compared with the ultrasonic flaw results of steel plates and previous study of inclusions distribution in slabs.

2. Mathematical Model Formulation

2.1. Flow and Turbulent Models

The fluid flow is based on the solution of the Navier-Stokes equations for incompressible viscous flow. The equations are generally given as follows:

$$\frac{\partial \rho}{\partial t} + \nabla \cdot \left(\rho \vec{u} \right) = 0 \quad \text{..... (1)}$$

$$\frac{\partial \left(\rho \vec{u} \right)}{\partial t} + \nabla \cdot \left(\rho \vec{u} \vec{u} \right) = -\nabla \cdot \tau_k - \nabla P + \rho g + S_i \quad \text{..... (2)}$$

The terms on the right-hand side of Eq. (2) are respectively representing the stress, the pressure gradient, gravity, and the momentum source term.

The stress term τ_k is described as follows:

$$\tau_k = -\mu_{eff} \left(\nabla \vec{u} + \left(\nabla \vec{u} \right)^T - \frac{2}{3} \mathrm{I} \left(\nabla \cdot \vec{u} \right) \right) \quad \text{..... (3)}$$

where μ_{eff} is the effective viscosity. The effective viscosity is composed of two contributions: molecular viscosity and turbulent viscosity.

$$\mu_{eff} = \mu + \mu_T \quad \text{..... (4)}$$

In the current work, the turbulent viscosity μ_T is calculated using the LES model. An important issue here is the selection of an appropriate SGS model. In the past, the model proposed by Smagorinsky[23] has been developed for calculating the turbulent viscosity μ_T.

$$\mu_T = \rho \left(C_S \Delta \right)^2 \left| S \right| \quad \text{..... (5)}$$

where C_S is the model constant with a value of 0.1. S is the characteristic filtered rate of strain, $S = \sqrt{2 S_{ij} S_{ij}}$, $S_{ij} = \frac{1}{2} \left(\frac{\partial u_i}{\partial x_j} + \frac{\partial u_j}{\partial x_i} \right)$, and $\Delta = \left(\Delta_i \Delta_j \Delta_k \right)^{1/3}$ is the filter width.

2.2. Solidification Models

The enthalpy-porosity approach is used to simulate the solidification of steel. It treats the liquid-solid mushy zone as a porous zone. The liquid fraction (0.0–1.0) is used to describe the mushy zone. The liquid fraction, β, can be defined as

$$\begin{cases} \beta = 1 & ,if \quad T > T_{liquidus} \\ \beta = \dfrac{T - T_{solidus}}{T_{liquidus} - T_{solidus}} & ,if \quad T_{solidus} < T < T_{liquidus} \\ \beta = 0 & ,if \quad T < T_{solidus} \end{cases} \quad \text{..... (6)}$$

The latent heat content can vary between 0 (for a solid) and 1.0 (for a liquid).

For solidification/melting problems, the energy equation is written as

$$\frac{\partial \left(\rho H \right)}{\partial t} + \nabla \cdot \left(\rho \vec{u} H \right) = \nabla \cdot \left(k \nabla T \right) + S_e \quad \text{..... (7)}$$

where H is the enthalpy of the material, S_e is source term of energy, $S_e = \rho L v_p (1 - \beta) - \rho L \frac{\partial \beta}{\partial t}$.

Here, v_p is the solid velocity due to the pulling of solidified material out of the domain (also referred to as the pull

velocity). The pull velocity is included to account for the movement of the solidified material as it is continuously withdrawn from the domain in continuous casting processes.

2.3. Particle Transport and Entrapment Models

The transient transport of particles is simulated based on the flow fields of LES inside the liquid pool. Due to the low volume fraction of particles, the Lagrangian approach is used to calculate the transport of argon bubbles and non-metallic inclusions. The motion of particles can be simulated by integrating the following transport equation for each particle, which considers contributions from eight different forces:

$$m_p \frac{dv_P}{dt} = F_G + F_B + F_P + F_D + F_L + F_{VM} + F_M + F_{Ma} \quad \text{....(8)}$$

The terms on the right hand side of Eq. (8) are gravitational force, buoyancy force, pressure gradient force, drag force, lift force, virtual mass force, Magnus force and thermal Marangoni force.

Marangoni force can be separated into thermal and solute terms. Mukai and Lin[14] proposed a Marangoni force acting on the spherical particles at the solidifying interface.

$$F_{Ma} = -\frac{2}{3}\pi d_p^2 \cdot \left(\frac{\partial \sigma}{\partial T}\frac{\mathrm{d}T}{\mathrm{d}x} + \frac{\partial \sigma}{\partial C}\frac{\mathrm{d}C}{\mathrm{d}x} \right) \quad \text{.....(9)}$$

Sahoo *et al.*[24] derived a model related with surface tension and temperature which is given by

$$\sigma = \sigma_0 - A(T - T_m) - RT\Gamma_o \ln(1 + k_o \alpha_o e^{-(\Delta H^o/RT)}) \quad \text{.....(10)}$$

where σ_0 is the surface tension of pure iron at the melting point, A is the temperature coefficient of surface tension of pure iron, T_m is the melting temperature of iron, R is the gas constant, Γ_o is the surface adsorption of sulfur at saturation, k_o is a constant related to the entropy of sulfur segregation, a_o is the sulfur content, ΔH^o is the standard heat of adsorption. The details can be seen in Sahoo's previous work.[24]

Other forces in the Eq. (8) are expressed as follows, and details can be seen in previous work.[16,25]

$$F_B + F_G = \frac{(\rho_p - \rho_l)\pi d_p^3}{6} g \quad \text{.....(11)}$$

$$F_P = \frac{\rho_l \pi d_P^3}{6}\frac{D\vec{u}}{Dt} \quad \text{.....(12)}$$

$$F_D = \frac{1}{8}\pi d_p^2 \rho_l C_D \left|\vec{u} - \vec{u}_p\right| \left(\vec{u} - \vec{u}_p\right) \quad \text{.....(13)}$$

$$F_L = C_L \cdot \frac{6K_s \mu_{eff}}{\rho_p \pi d_p} \left(\frac{\rho_l}{\mu_{eff}} \right)^{1/2} \cdot \left(\vec{u} - \vec{u}_p\right) \quad \text{.....(14)}$$

$$F_{VM} = C_{VM} \cdot \frac{\pi \rho_l d_p^3}{12} \left(\frac{D\vec{u}}{Dt} - \frac{D\vec{u}_p}{Dt} \right) \quad \text{.....(15)}$$

$$F_M = C_M \cdot \frac{3\rho}{4\rho_p d_p} \left|\vec{u} - \vec{u}_p\right| (\vec{u} - \vec{u}_p) \quad \text{.....(16)}$$

When the temperature of steel is higher than liquidus temperature (1 786 K), particles can travel inside the liquid pool, and the motion of particles is governed by the gravitational force, buoyancy force, pressure gradient force, drag force, lift force, virtual mass force and Magnus force. However, when the particles are pushed to the mushy-zone, where the temperature is between liquidus temperature and solidus temperature (1 730 K), in addition to the forces described above, and one extra force is exerted on a particle that is the Marangoni force. According to the works of Yamazaki *et al.*[26] and Zhang *et al.*,[27] in the current study, it is assumed that particles would be entrapped if the liquid fraction at the location of particles is below 0.6.

2.4. Boundary Condition and Solution Method

In the current work, the coupled model is solved using the software of Fluent 14.0 combined with user defined function (UDF) to describe the transient turbulent flow, solidification, and particle transport and entrapment in the continuous casting mold. The computational domain includes the SEN, entire mold, and part of the secondary cooling zone (includes entire vertical section and part of curved section). Each section has different cooling conditions. The geometrical schematic and heat transfer boundary conditions are given in **Fig. 2**. A uniform velocity for molten steel is prescribed at the inlet based on the casting speed. For computing the pull velocities: at a velocity inlet, a stationary wall, or a moving wall, the specified velocity is used; at all other boundaries (including the liquid-solid interface between the liquid and solidified material), a zero-gradient velocity is used. The whole domain is divided to be 1.5×10^6 finite volumes. The time step size is 2.5×10^{-4} seconds.

Dispersed argon bubbles and non-metallic inclusions with sizes of 50 and 100 μm are injected randomly into the SEN from the inlet. The same number for each size class is 3000. The initial locations are uniformly distributed at the inlet surface. It is assumed that particles are reflected once touching the walls inside and outside the SEN, and escape once reaching the top surface, and leave the system once entering the bottom of the domain. The effects of turbulence are considered in particles traces using the "random walk model".

3. Inclusions Distribution of *In Situ* Observation

In order to investigate the inclusion distribution in the slabs obtained from this calculating mold, the *in situ* ultrasonic testing (UT) of rolled steel plate is carried out. Before slabs were rolled, they had been handled with slab scarfing machine, surface defects (contain inclusions) have been removed. **Figure 3** shows the inclusions distribution inside

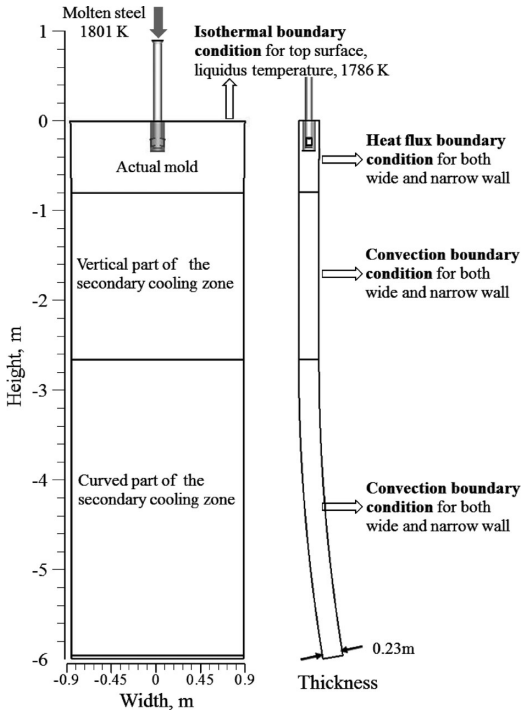

Fig. 2. Schematic of the calculation model and boundary conditions.

two steel plates along with the three cross-sections of the plate (casting direction section, transverse section, and side section respectively), which are obtained from the same vertical-bending continuous caster at different times. As can be observed from the visual analysis, the etch-pits, viewed as green dots are the entrapped argon bubbles and non-metallic inclusions. In Fig. 3(a), along the casting direction section, it can be seen that there is no inclusion on the right side of the steel plate; many inclusions are located at the lower part of the steel plate. A macro inclusion (a large bubble and many attached no-metallic inclusions) is found inside the steel plate. Compared with the result of Fig. 3(a), the number of inclusions increases, in Fig. 3(b), more inclusions are found inside the steel plate and the distribution is uniform along the casting direction section. Compared the two images, it can be found that the distribution of inclusions is intermittent, unsteady and asymmetrical, suggesting that they are related to the transient flow structures. Due to the surface scarfing, very few inclusions can be seen at the steel plate surfaces. As is obvious, high particle numbers are found mostly at 1/4 and 1/2 thickness of the steel plates, forming an obvious inclusions band along the casting direction and width direction, respectively. However, few particles were found in the regions adjoining the surfaces of steel plates. Another visual observation in thickness direction, most of inclusions locate at one side of the steel plate. According to the structure of the vertical-bending continuous caster and the buoyancy of inclusion, it can be judged that this side is the inner-curved section of the mold.

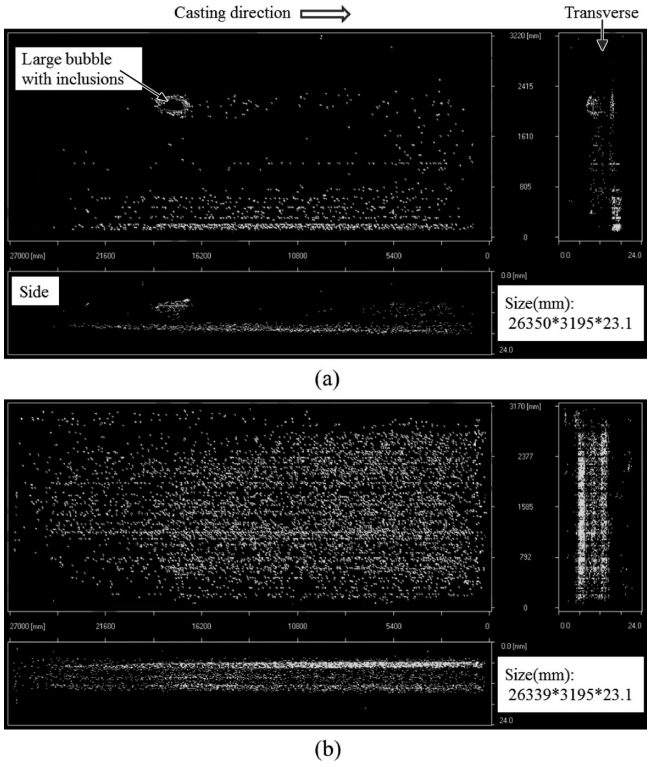

Fig. 3. Ultrasonic testing of different rolled steel plates.

4. Results and Discussion

4.1. Flow Pattern and Solidification

The fluid flow pattern determines the temperature and liquid fraction distributions of molten steel in the mold. And it is also important to the internal cleanliness and quality of the steel. **Figures 4**(a) and 4(b) show the fluid flow patterns inside the mold through dye-injection observation of water model experiments at different times for the same operation, which are obtained from author previous work.[28] The normal Froude similarity number (Fr) and the modified Froude similarity number (Fr_g) were used to obtain the water flow rate and air flow rate of the water model, respectively, as shown in Eqs. (17) and (18). And the increase in volume during heating of the injected argon gas (25°C) to molten steel temperature (1 530°C) has been considered. The ratios of water-steel flow rates and air-argon gas flow rates have been shown in Eqs. (19) and (20). Here, the water flow rate was 40.08 L/min; and the air flow rate was 3.34 L/min. Details can be seen in author previous work.[28] It can be seen that the flow pattern inside the mold was not symmetric and not stationary. The left recirculation domain in the lower recirculation zone was much bigger than the right one in one of the repeated experiments, as shown in Fig. 4(a). After some time, in Fig. 4(b), it changed and became a mirror image of the previous one.

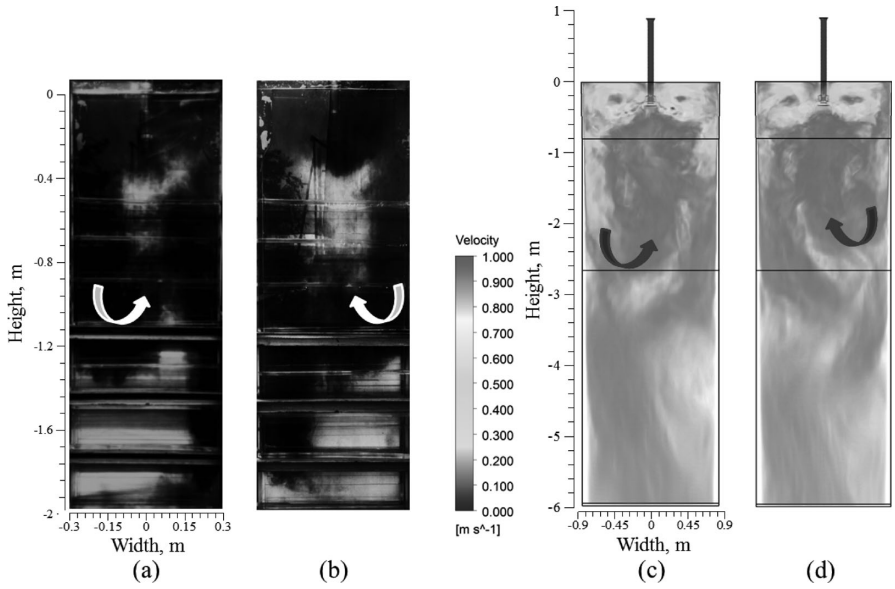

Fig. 4. Asymmetrical flow pattern obtain from the water model experiment ((a) and (b)) and the LES model ((c) and (d)) at different times.

$$Fr = \left(\frac{u^2}{gl}\right)_{water} = \left(\frac{u^2}{gl}\right)_{steel} \quad \text{..... (17)}$$

$$Fr_g = \left(\frac{\rho_g u^2}{(\rho_l - \rho_g) gl}\right)_{air} = \left(\frac{\rho_g u^2}{(\rho_l - \rho_g) gl}\right)_{\arg on} \quad \text{.... (18)}$$

$$Q_{water} = 0.06415 Q_{steel} \quad \text{..... (19)}$$

$$Q_{air,25°C} = 0.1026 Q_{\arg on,25°C} \quad \text{..... (20)}$$

Figures 4(c) and 4(d) show the predicted transient volume velocity field inside the liquid pool at different times of 100 and 135 seconds, respectively. The LES results further reveal the significant flow asymmetry in the lower recirculation zone of the mold. This asymmetry is caused by the unbalanced flow between the two halves of the lower zone. At the time of 100 s, in Fig. 4(c), the left recirculating domain is much bigger than the right one. But at 135 s, in Fig. 4(d), just the opposite is happening, the right recirculating domain is much bigger than the left one. The shape of the upper and lower recirculation zones agrees well with the dye-injection observation (as shown in Figs. 4(a) and 4(b)). So the LES model proved to be very useful to study the transient asymmetrical flow inside the liquid pool.

Growth of the solidified shell naturally depends on casting conditions (flow pattern of molten steel) and cooling conditions (interfacial and superheat fluxes). In order to study the solidified shell growth dynamic, the liquid fraction magnitudes of steel at different positions below the meniscus were predicted, as shown in **Fig. 5**(a). The variable ranges from 0.0 to 1.0, where 0.0 represents a total solidification and 1.0 represents full molten steel. It should be noticed that the thickness of solidified shell increased with the strand length. In the current work, it was assumed that particles would be entrapped at the location where the local liquid fraction is 0.6. So the iso-surface of 0.6 liquid fraction has been shown in Fig. 5(b). According to the hypothesis, the particles would keep moving inside this iso-surface and stop moving at this iso-surface.

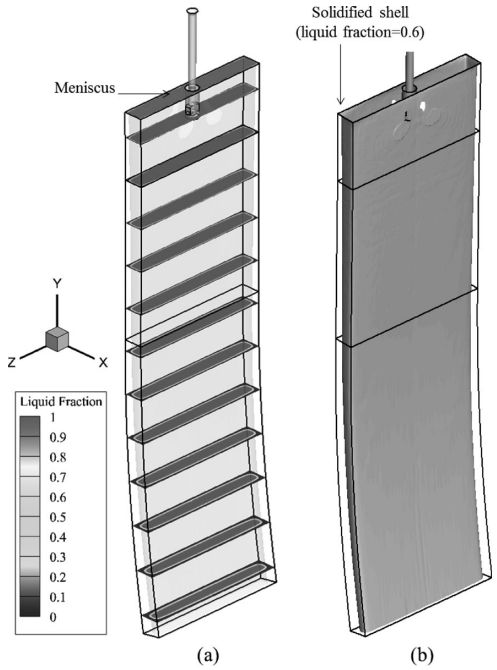

Fig. 5. Liquid fraction distribution at different planes (a) and iso-surface of 0.6 liquid fractions (b).

Figure 6 compares the predicted thickness of solidified shell using this model and the perfect parabolic law according to the well known relationship: $s = K\sqrt{t}$.[29] Considering the crude nature of the measuring apparatus and the many model assumptions. The model reasonably predicts the trend of the thickness of solidified shell over the entire domain. From the result, it can be seen that the calculated thicknesses of solidified shell agree well with the simple expression (K = 27.5). Due to the hot molten steel jet impinges against the solidifying shell, the solidified shells are thinner (remelting phenomenon) near the SEN port and on the narrow face about 0.25 m below the meniscus. The thickness of solidified shell at the three referenced locations, yield an average value of 17 mm at the actual mold end (0.8 m below top surface); 32 mm at the curved part of the secondary cooling zone (2.7 m below top surface); 48 mm at the outlet of the calculated domain. The thickness of solidified shell is very important, because it controls the entrapment positions of bubbles and inclusions.

4.2. Particle Transport in the Liquid Pool

Understanding the asymmetrical flow pattern of molten steel is important, but further study the associated phenomena such as particle motion and entrapment are more practical. The obtained flow field of molten steel at 100 seconds was used as initial field to investigate the particle behaviour inside the liquid pool. Two groups of argon bubbles (50 and 100 μm) and two groups of inclusions (50 and 100 μm) were injected randomly into the SEN from the inlet for one second (100 to 101 s).

In order to observe the transient distribution of particles inside the liquid pool with time, the motion of the 50 μm non-metallic inclusion is illustrated in **Fig. 7**. The casting speed is also 1.2 m/min, and without considering the effect of argon gas injection on the flow pattern. Non-metallic inclusions are respresented with red sphere. At 1.5 second after injection, in Fig. 7(a), it can be observed that all the inclusions follow the high-speed downward jet in the SEN, and then they are split into two parts, corresponding to the jet flow. 1.5 seconds later, some of them can rise to the meniscus and are removed, as shown in Fig. 7(b). By 10 seconds after injection (Fig. 7(c)), many inclusions are well-dispersed throughout the upper recirculation zone of the mold, and others are branched forming two downward streams of particles. At 30 seconds after injection, in Fig. 7(d), some inclusions have moved to the curved part of the secondary cooling zone. By 100 seconds after injection (Fig. 7(e)), some inclusions have flowed out of the calculated domain, and it is difficult for these inclusions to float to the top surface again, so they would be continue moving inside the deeper liquid pool and captured at some deeper locations

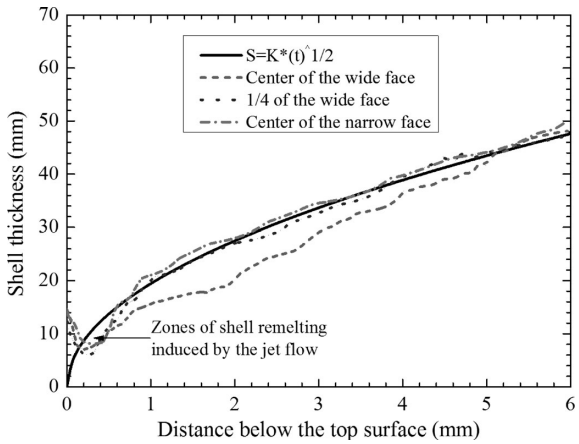

Fig. 6. The growth of solidified shell.

of this caster.

Although the distribution of inclusions is symmetric about the SEN in the upper recirculation zone at approximately 10 seconds, a noticeable asymmetry in the lower recirculation zone is seen at 30 seconds and 100 seconds, which is caused by the asymmetrical flow in the liquid pool. So the transport of particles depends obviously on the flow pattern.

4.3. Entrapment Positions of Particles

In the current work, based on the transient flow fields and the balance of the eight different forces which act on the particle in the boundary layer region, particles touch the solidification front (liquid fraction=0.6) are always assumed to become entrapped, and the number of entrapped particles and the position of every entrapped particle are recorded using the UDF of Fluent. **Figure 8** shows the distributions of entrapment positions of 50 μm non-metallic inclusions at different times, which are obtained from the width direction and thickness direction, respectively. The entrapped inclusions are represented with red dots. Corresponding to Fig. 7(a), at 1.5 seconds, some inclusions are found in the regions near the SEN and adjoining the slab surface, as shown in Fig. 8(a). 3 s after injection, in Fig. 8(b), more inclusions are entrapped along the jet directions. With the development of time, 10 s later (Fig. 8(c)), many inclusions had been entrapped at the upper region of the mold, and some of them are located adjoining the narrow face of the mold from the thickness direction, because the shell thickness at wide face of the mold is thin. At 30 seconds, in Fig. 8(d), several inclusions had been found at the curved part of the secondary cooling zone. Most of entrapped inclusions are located within the scope of 1 m below the top surface, less entrapped inclusions are found at the lower region of the domain. By 100 s after injection (Fig. 8(e)), more inclusions are entrapped at the curved part of the secondary cooling zone of the mold, and due to the buoyancy of inclusion, more of them are located at the inner-curved section of the mold. For the current model, the predicted inclusion distribution agrees well with measured data of UT at the rolled steel plates (Fig. 3).

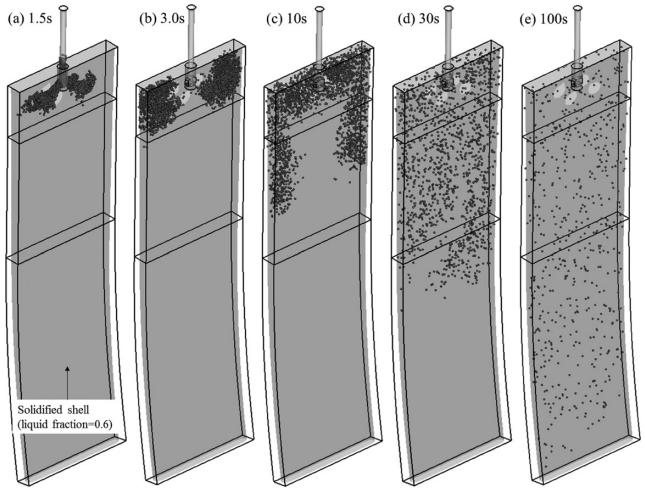

Fig. 7. Transient distributions of 50 μm non-metallic inclusions inside the liquid pool of the mold.

Figure 9(a) shows the 50 μm non-metallic inclusion distribution in the cross section of the mold after 150 seconds injection, including the entrapped inclusions by solidified

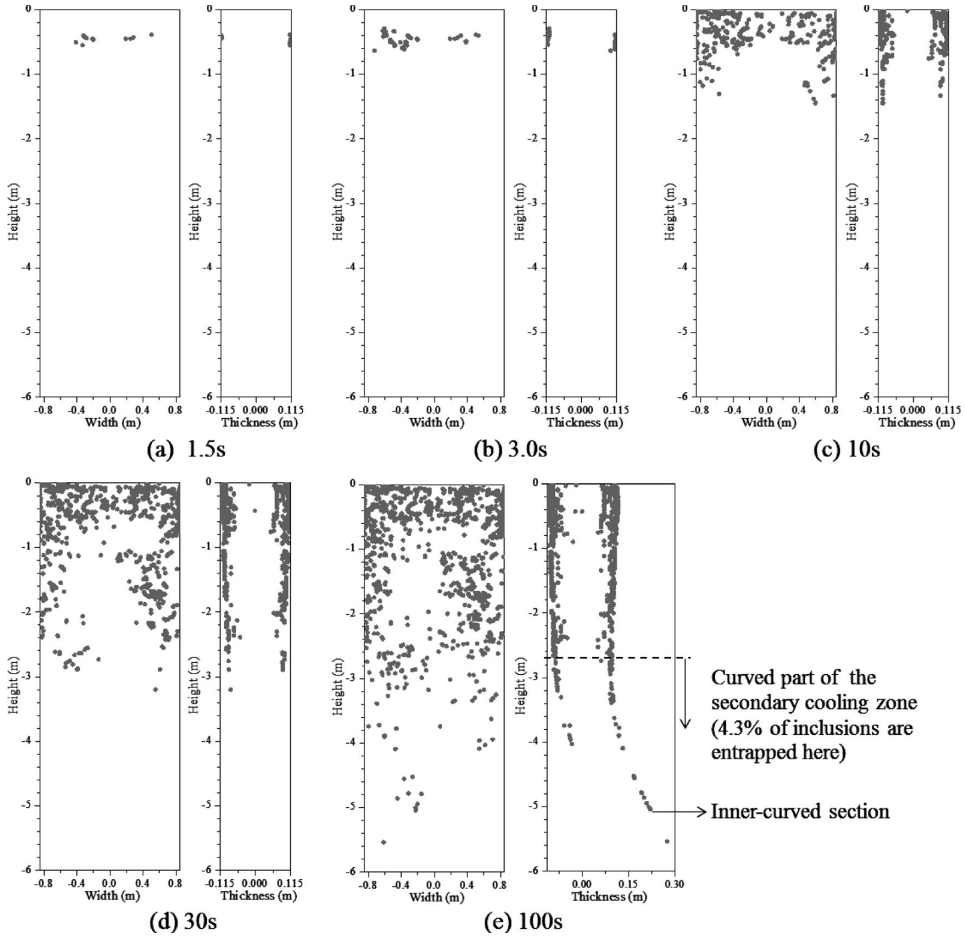

Fig. 8. Transient entrapment positions of 50 μm inclusions in solidified shell.

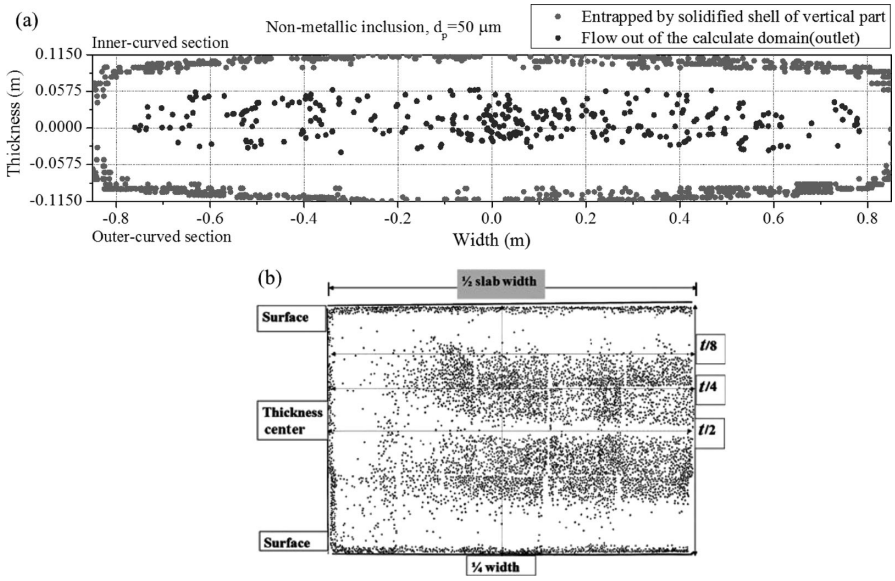

Fig. 9. Distributions of 50 μm inclusions in the cross-section (a) and previous measured data of inclusions locations in a slab cross-section (b).[21)]

shell of vertical part and the inclusions of flowing out of the bottom. The entrapped inclusions are represented with red dots which located near the wall of the mold, and the inclusions of flowing out are represented with blue dots which located in the center of the mold. This result indicates that most of the captured inclusions are entrapped within the solidified shell approximately 3 to 15 mm beneath the width face, and some captured inclusions are found 15 to 30 mm beneath the width face near the narrow face and 0 to 50 mm beneath the narrow face. Finally, a few inclusions flow out of the bottom with the outflow and would continue moving inside the liquid pool and be captured at a deeper location of the caster. Their final positions at the outlet are recorded, as shown in blue dots. The result indicates that the predicted local distribution of inclusions at the bottom of the domain is not symmetrical, more of these inclusions located at the inner-curved section. These positions somehow correspond to the final entrapment positions of inclusions in the solidified slab. The predicted results agree well with the previous measured data of inclusions distribution in commercial aluminum DC-cast slab, in Fig. 9(b), which was obtained using a deep-etching method by Jaradeh and Carlberg.[21)] As can be seen from the visual analysis, the etch-pits, viewed as black dots are the non-metallic inclusions. The size of cross-section of this slab is 1 440×460 mm (width×thickness). The figure shows half of a slice cut through the whole ingot. It can be observed from the figure, different regions of high and low inclusion numbers can be distinguished clearly. The inclusion population is highest near the slab surface (within 13 mm of the slab surface) and at 120–150 mm away from slab surface in the thickness direction (around t/4, t = thickness of slab). However, few inclusions are found in the regions of 50 to 100 mm from the slab surface in the thickness direction and the slab thickness centerline.

4.4. Statistics of Particles Entrapment

The above results clearly demonstrated the transient asymmetrical particle transport inside the liquid pool, and entrapped positions of particles using the coupled computational model. But the statistical prediction of the entrapment of particles in the solidified slab would be more helpful for removing the particles and improving the quality of the slab. In this section, the statistics of particles entrapment are studied, considering the effect of particle size and the difference between argon bubbles and non-metallic inclusions.

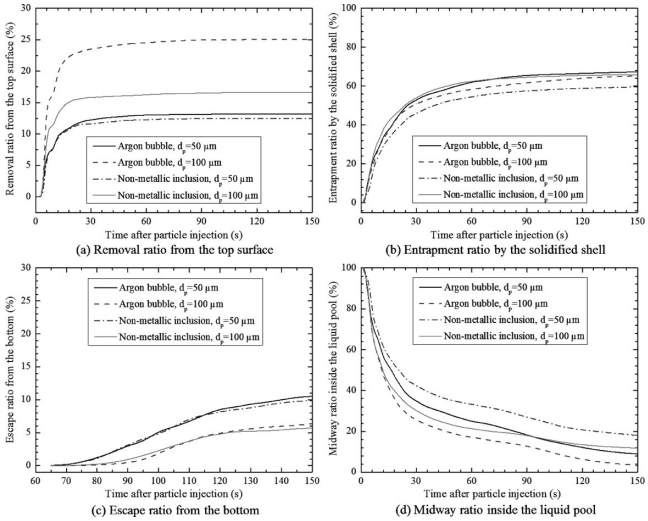

Fig. 10. Predicted transport and entrapment histories of different particles.

Figure 10 shows the transport and entrapment histories of different particles. Four aspects are analyzed: removal ratio from the top surface, entrapment ratio by the solidified shell, escape ratio from the bottom of the computational domain, and midway ratio inside the liquid pool (still moving inside the liquid pool until the end of the calculation). It can be found that most particles are removed from the top surface within 20 seconds, as shown in Fig. 10(a). Concentrated periods for particles to be entrapped by the solidified shell are 3 s–20 s and 20 s–90 s, in Fig. 10(b), which indicates that some particles are directly entrapped during transport in the upper recirculation zone with jet, others are taken deeper into the lower recirculation zone, stay for some time, and then gradually be entrapped by solidified shell. From the Fig. 10(c), it can be seen that some particles could escape from the bottom of the domain until 65 seconds after injection. There are still some particles moving inside the liquid pool until the end of the calculation, especially for 50 μm non-metallic inclusion, the midway ratio is about 18%, as shown in Fig. 10(d). The results also show that the removal ratio increases, entrapment ratio, escape ratio, and midway ratio decreases with increasing particle diameter. Compared

with the non-metallic inclusion, argon bubble with the same diameter is easier to be removed and entrapped.

In order to analyze the statistical inclusion entrapment position, three parts were selected (height, width, and thickness of calculation domain). These parts are divided into 30 equal zones, respectively. **Figure 11** shows the predicted local entrapment ratios of argon bubbles and non-metallic inclusions along the height direction (various distances below the top surface) at 150 seconds after injection. It can be observed that most particles are entrapped within the shell approximately 0 to 0.8 m below the top surface (corresponding to a shell thickness of 0 to 17 mm). Few particles are entrapped at the curved part of the secondary cooling zone, 2.7 to 6 m below the top surface (corresponding to a shell thickness of 32 to 48 mm).

Figure 12 shows the predicted local entrapment ratios of argon bubbles and non-metallic inclusions along the width direction at 150 seconds after injection. Most entrapped particles are found at the regions of 0.2 to 0.85 m from the center (0.0). The peak of entrapped particle number is observed near the narrow face of the mold, which is due to many inclusions are located approximately 15 to 30 mm beneath the width face near the narrow face, and some inclusions are entrapped 0 to 50 mm beneath the narrow face, as shown in Fig. 9(a). Several high numbers of entrapped particles can be observed around the locations of –0.4, –0.65 and 0.65 m. But few particles are entrapped at the regions of –0.2 to 0 m (center) and 0 to 0.2 m. At the width direction, the entrapment positions of particles are not symmetric. For 50 μm argon bubbles, more bubbles (37.93%) can be entrapped at the left side of the domain. Conversely, more particles are entrapped at the right side (35.5, 29.97, and 36 pct. for 100 μm argon bubbles, 50 μm and 100 μm non-metallic inclusions, respectively).

Figure 13 shows the predicted local entrapment ratios of argon bubbles and non-metallic inclusions along the thickness direction at the vertical part of the mold. For all the types of particles, it can be noted that most of the entrapped particles are located at the regions of –0.115 to –0.069 m and 0.069 to 0.115 m, with a peak in number of particles at the inner-curved surface of the slab. Along the thickness direction, the entrapment positions of particles are not symmetric as well. Furthermore, few particles are entrapped by the solidified shell of thickness center at the vertical part (corresponding to the shell in the center of narrow face). It may be due to the "washing effect" of hot steel jet flow, by which the strong flow velocity at the solidification front near the narrow face suppresses entrapment.

Few particles are entrapped at the current curved part of the domain, for example, there is only 4.3 pct. of 50 μm non-metallic inclusions are entrapped here, as shown in Fig. 8(e). But approximately 10 pct. of 50 μm non-metallic inclusions can escape from the bottom, so it is essential to study the local distributions of particles at the bottom of the domain, because these particles will be entrapped at the deeper locations of the caster. **Figure 14** shows the predicted local escape ratios of argon bubbles and non-metallic inclusions at the bottom. It is very obvious that more parti-

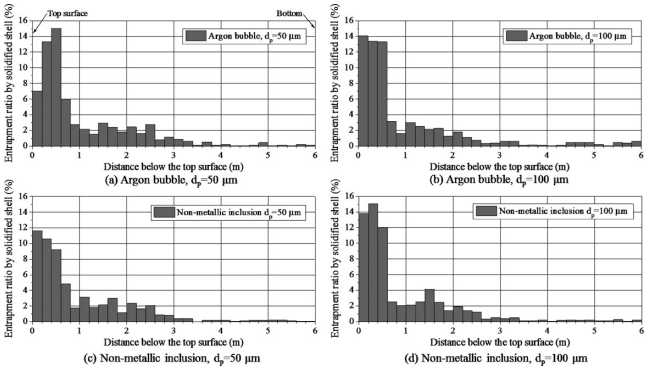

Fig. 11. Predicted local entrapment ratios of different particles along the height direction.

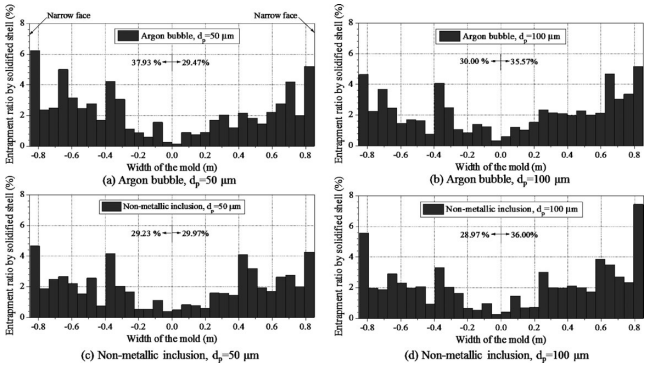

Fig. 12. Predicted local entrapment ratios of different particles along the width direction.

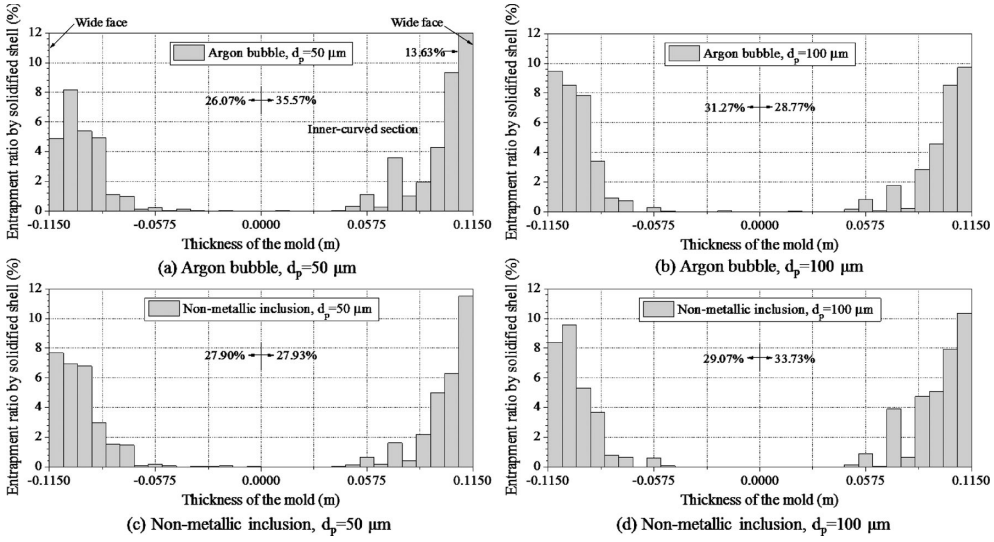

Fig. 13. Predicted local entrapment ratios of different particles along the thickness direction.

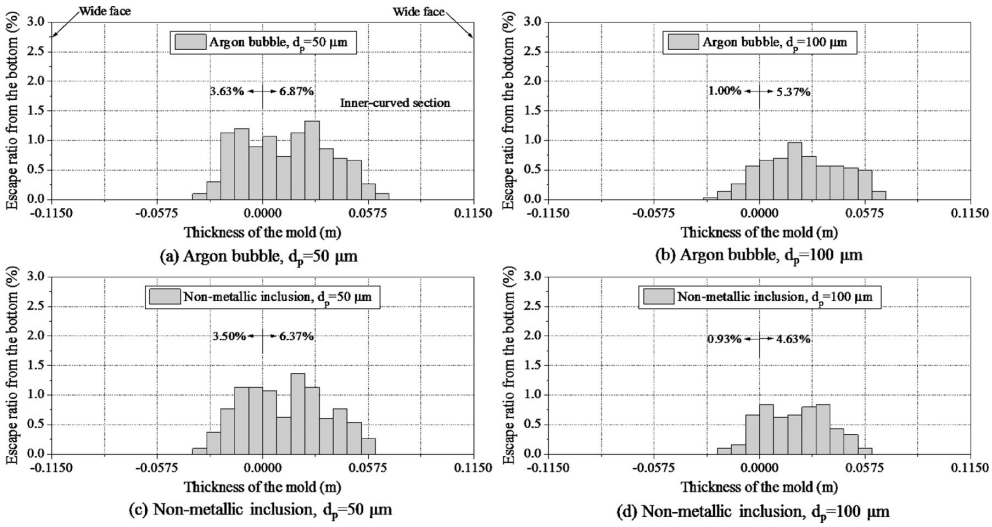

Fig. 14. Predicted local escape ratios of different particles from the bottom of the domain.

Table 1. Thermo-physical properties and boundary conditions for the simulation.

Parameters	Value
Casting speed, $m \cdot min^{-1}$	1.2
Molten steel density, $kg \cdot m^{-3}$	7 020
Argon bubble density, $kg \cdot m^{-3}$	0.56
Non-metallic inclusion density, $kg \cdot m^{-3}$	2 700
Molten steel viscosity, $kg \cdot m^{-1} \cdot s^{-1}$	0.0056
Specific heat at constant pressure, $J \cdot kg^{-1} \cdot K^{-1}$	710
Enthalpy of fusion, $kJ \cdot kg^{-1}$	270
Solidus temperature, K	1 730
Liquidus temperature, K	1 786
Initial temperature, K	1 801
Heat flux on wide and narrow face of the actual mold, $W \cdot m^{-2}$	$q = 2.68 - \psi\sqrt{60h_m / V_C}$
Average heat transfer coefficient for wide face of the secondary cooling zone, $W \cdot m^{-1} \cdot K^{-1}$	350
Average heat transfer coefficient for narrow face of the secondary cooling zone, $W \cdot m^{-1} \cdot K^{-1}$	300

cles can escape from the inner-curved section (6.87, 5.37, 6.37, and 4.63 pct. for 50, 100 μm argon bubbles and 50, 100 μm non-metallic inclusions, respectively). Through comparing the number of particles escaping from outer-curved section and inner-curved section, it can be seen that larger particles would escape from the inner-curved section more easily. According to all the above results, four different types of particles have approximate entrapment and escape positions, just with different entrapment ratios.

5. Conclusions

The mathematical model developed in the current study has been carried out for investigating the transient turbulent flow, solidification, and transport and entrapment of particles in the continuous casting mold. The conclusions are as follows:

(1) The distributions of argon bubbles and non-metallic inclusions in the industrial rolled steel plates are intermittent and asymmetric.

(2) The transient flow pattern inside the liquid pool of the mold is asymmetric, the shapes of the upper and lower recirculation zones agree well with the dye-injection observations of water model experiments.

(3) The transient distribution of particles inside the liquid pool is asymmetric in the lower recirculation zone, which are associated with the asymmetrical molten steel flow.

(4) Most particles are entrapped within the solidified shell approximately 3 to 15 mm beneath the slab width face. Some entrapped inclusions are found 0 to 50 mm beneath the slab surface near the narrow face. A few particles flow out of the bottom with the outflow and would continue moving inside the deeper liquid pool. The predicted local distribution of particles at the bottom is not symmetric, more of them located at the inner-curved section. These positions somehow correspond to the final entrapment positions of particles in the solidified slab. The predicted results agree well with the measured data of inclusion distributions at industry slab and rolled steel plates.

(5) Most particles are removed from the top surface within 20 seconds. Concentrated periods for particles to be entrapped by the solidified shell are 3 s–20 s and 20 s–90 s. Some particles can escape from the bottom until 65 seconds after injection.

(6) From the height direction, most particles are entrapped within the shell approximately 0 to 0.8 m below the top surface; few particles are entrapped at the curved part of the secondary cooling zone, 2.7 to 6 m below the top surface. From the width direction, most entrapment particles are found at the regions of –0.85 to –0.2 m and 0.2 to 0.85 m; few particles are entrapped at the regions of –0.2 to 0 m and 0 to 0.2 m. From the thickness direction, most particles are entrapped at the regions of –0.115 to –0.069 m and 0.069 to 0.115 m, with a peak in number of particles at the inner-curved surface of the slab. More particles escape from the bottom at the inner-curved section of the domain.

(7) The removal ratio increases, entrapment ratio, escape ratio and midway ratio decreases with increasing particle diameters. Compared with the non-metallic inclusion, argon bubble with the same diameter is easier to be removed and entrapped. All four different types of particles have approximate entrapment positions, just with different entrapment percent.

Acknowledgements

Authors are grateful to the National Natural Science Foundation of China for support of this research, Grant No. 51210007.

Nomenclature

a_o: Oxygen constant
A: Temperature coefficient of surface tension of pure iron
C: Solute concentration
C_D: Drag coefficient
C_L: Lift force model constant
C_{VM}: Virtual mass force model constant
C_M: Magnus force coefficient
C_S: Sub-grid scale model constant
d_p: Particle diameter
F_B: Buoyancy force
F_D: Drag force
F_G: Gravitational force
F_L: Lift force
F_M: Magnus force
F_{Ma}: Marangoni force
F_p: Pressure gradient force
F_{VM}: Virtual mass force
g: Acceleration of gravity
h_m: Distance below the meniscus
H: Enthalpy
I: Unity tensor
k: Thermal conductivity
k_o: Constant related to the entropy of oxygen segregation
K: Constant
l: Characteristic length
L: The latent heat of the material
m_p: Mass of particle
P: Pressure
q: Heat flux
Q: Volume flow rate
R: Gas constant
S: Characteristic filtered rate of strain
S_e: Energy source term
S_i: Momentum source term
t: Time
T: Temperature
$T_{liquidus}$: Liquidus temperature
T_m: Melting temperature of iron
$T_{solidus}$: Solidus temperature
$\vec{u}$: Velocity of molten steel
$\vec{u}_p$: Velocity of particle
V_C: Casting speed
α_k: Volume fraction of k phase
α_g: Volume fraction of gas phase
β: Liquid fraction
ρ: Density
μ_{eff}: Effective viscosity
μ_T: Turbulent viscosity
μ: Molecular viscosity
Δ: Filtering width
Δ_i: Grid spacing in X direction
Δ_j: Grid spacing in Y direction
Δ_k: Grid spacing in Z direction
ΔH^o: Standard heat of adsorption
τ: Shear stress
v_p: Pulling velocity
ψ: Constant
σ: Surface tension
Γ_o: Surface adsorption of oxygen at asturation
Fr: Froude similarity number
Fr_g: Modified Froude similarity number

REFERENCES

1) B. G. Thomas: *AIST Trans.*, **3** (2006), 128.
2) Y. Miki and S. Takeuchi: *ISIJ Int.*, **43** (2003), 1548.
3) L. F. Zhang and B. G. Thomas: *ISIJ Int.*, **43** (2003), 271.
4) K. H. Tacke: *J. Iron Steel Res. Int.*, **18** (2011), 211.
5) L. Wang, H. G. Lee and P. Hayes: *ISIJ Int.*, **36** (1996), 17.
6) J. S. Cho and H. G. Lee: *ISIJ Int.*, **41** (2001), 151.
7) Y. J. Kwon, J. Zhang and H. G. Lee: *ISIJ Int.*, **46** (2006), 257.
8) T. Watanabe and M. Iguchi: *Tetsu-to-Hagané*, **94** (2008), 1.
9) Q. Yuan, B. G. Thomas and S. P. Vanka: *Metall. Mater. Trans. B*, **35** (2004), 703.
10) Y. F. Wang, A. P. Dong and L. F. Zhang: *Steel Res. Int.*, **82** (2011), 428.
11) M. D. Santis and A. Ferretti: *ISIJ Int.*, **36** (1996), 673.
12) M. R. Aboutalebi, M. Hasan and R. I. L. Guthrie: *Metall. Mater. Trans. B*, **26** (1995), 703.
13) Z. Q. Liu, B. K. Li and M. F. Jiang: *Metall. Mater. Trans. B*, **45** (2014), 675.
14) K. Mukai and W. Lin: *Tetsu-to-Hagané*, **80** (1994), 527.
15) K. Mukai and W. Lin: *Tetsu-to-Hagané*, **80** (1994), 533.
16) K. Mukai, L. C. Zhong and M. Zeze: *ISIJ Int.*, **46** (2006), 1810.
17) T. Miyake, M. Morishita, H. Nakata and M. Kokita: *ISIJ Int.*, **46** (2006), 1817.
18) S. M. Lee, S. J. Kim and H. G. Lee: *J. Iron Steel Res. Int.*, **18** (2011), 220.
19) B. G. Thomas, Q. Yuan, S. Mahmood, R. Liu and R. Chaudaary: *Metall. Mater. Trans. B*, **45** (2014), 22.
20) Y. Miki, H. Ohno, Y. Kishimoto and S. Tanaka: *Tetsu-to-Hagané*, **97** (2011), 17.
21) M. M. Jaradeh and T. Carlberg: *Metal. Mater. Trans. B*, **43** (2012), 82.
22) Z. Q. Liu, B. K. Li, M. F. Jiang and F. Tsukihashi: *ISIJ Int.*, **53** (2013), 484.
23) J. Smagorinsky: *Monthly Weather Rev.*, **91** (1963), 99.
24) P. Sahoo, T. Debroy and M. J. Mcnalla: *Metall. Mater. Trans. B*, **19** (1988), 483.
25) B. K. Li, T. Okane and T. Umeda: *Metall. Mater. Trans. B*, **32** (2001), 1053.
26) M. Yamazaki, Y. Natsume, H. Harada and K. Ohsasa: *ISIJ Int.*, **46** (2006), 903.
27) L. F. Zhang, Y. F. Wang, E. Martinez and K. D. Peaslee: CFD Modeling and Simulation in Materials, TMS, Warrendale, PA, (2012), 3.
28) Z. Q. Liu, B. K. Li, M. F. Jiang, L. Zhang and G. D. Xu: *Acta Metal. Sin.*, **49** (2013), 513.
29) K. J. Schwerdtfeger: The Making, Shaping and Treating of Steel, Casting Volume, AIST, Warrendale, PA, (2003), 85.